PAPER

An optical backscatter probe for time resolved droplet measurements in turbomachines

IOP Publishing Measurement Science and Technology
Meas. Sci. Technol. **27** (2016) 015204 (19pp) doi:10.1088/0957-0233/27/1/015204

An optical backscatter probe for time resolved droplet measurements in turbomachines

Ilias Bosdas[1], Michel Mansour[1], Anestis I Kalfas[2] and Reza S Abhari[1]

[1] Laboratory for Energy Conversion, Department of Mechanical and Process Engineering, ETH Zurich, Zurich, Switzerland
[2] Department of Mechanical Engineering, Aristotle University of Thessaloniki, Greece

E-mail: ibosdas@ethz.ch

Received 16 July 2015, revised 1 October 2015
Accepted for publication 9 October 2015
Published 1 December 2015

Abstract

The presence of particles in the flow path of turbomachines can result in undesirable engine operation. In order to improve the efficiency of turbomachines and guarantee their safe operation, the flow mechanisms that govern the particles' need to be studied and associated with the main aerodynamic flow field. This paper describes a newly developed optical backscatter probe for droplet diameter and speed measurements in turbomachines. The miniature probe has a tip diameter of 5 mm and is capable of resolving droplets from 40 to 110 μm in diameter that travel up to 200 m s^{-1}. The calibration of the novel probe is performed with a droplet generator capable of producing monodispersed water droplets. In addition, the probe is calibrated for droplet speed measurements in the same calibration facility. The paper conducts a detailed uncertainty analysis and describes the post processing code. In the final part of this paper the probe is used in an axial turbine with an installed spray generator to perform droplet measurements under two different operating conditions. Measurements have shown that the part load condition results in larger droplet diameters and higher relative droplet speeds. As a consequence higher erosion rates at the rotor leading edge suction side will occur when operating at part load condition.

Keywords: Coarse water droplets, optical probe, time resolved measurements, blade erosion, steam turbine, spray

(Some figures may appear in colour only in the online journal)

Nomenclature

I	Light intensity [Watts m^{-2}]
θ	Scattering angle [deg]
c	Stator's chord [mm]
x	Stator's axial downstream location [mm]
D	Diameter [μm]
t	Time [s]
U	Velocity [m s^{-1}]
fg	Droplet frequency generator [kHz]
We	Weber number [-]
R	Erosion Rate [-]
r	Radius [mm]
E	Extinction coefficient [-]
N	Distribution [-]
m	Refractive index [-]
L	Distance [mm]
PA	Pulse Amplitude [mV]
Ma	Mach Number [-]

Greek

λ	Wavelength [μm]
σ	Surface tension [N m^{-1}]

ρ	Density [kg m^{-3}]
ω	Rotational speed [rad s^{-1}]
τ	Turbidity [cm^{-1}]

Subscripts

res	Residence
abs	Absolute
rel	Relative
f	Flow
d	Droplet
eff	Effective
avg	Average value
10	Arithmetic mean diameter
32	Sauter mean diameter
M	Most frequent value in a data set (i.e. diameter)
e	Erosion
o	Incident light intensity

1. Introduction

Optical techniques are extensively used in droplet measurements in many scientific fields including turbomachinery [1]. The first reported attempts to measure droplets in atmospheric research were conducted in the 1970s. Since then several research groups have reported their efforts to measure droplet sizes in the range of 0.1 up to 1000 μm and for droplet concentrations of up to 500 cm^{-3} using optical probes mounted on test flight aircrafts in order to improve weather models [2–7]. These probes mainly utilize light scattering and imaging techniques, but their large size ($D_d > 300$ mm) and specific geometry are not suitable for turbomachinery applications. In addition, the measurement of droplet size distribution in two-phase flows is of high interest to combustion science, dusty plasma physics and medicine science. In order to understand the factors that govern droplet size distribution and motion, different types of instruments have been developed in these fields and presented in [8–10] but never in a compact size of a miniature probe type.

The presence of particles in the flow path of gas turbines can result in several issues related to the machines' operation. Volcanic ash, ice and subcooled water ingestion or wet compression involves particles or droplets in the flowpath of turbomachines. The main impacts are ash deposition on blades, degradation of the cooling system, compressor blade fouling and reduction of blade aerodynamic efficiency, which can lead to premature engine failures [11–14]. In addition, the increased share of renewable energies with the use of turbomachines has also brought special attention to the topic. Turbomachinery applications in renewable power generation include geothermal power and concentrated solar power (CSP) operated with the Rankine cycles. The steam turbines used in geothermal power plants typically operate with a low inlet temperature of 180 °C, and condensation phenomena in the last stages of low-pressure steam turbines produce a dense fog of water droplets with a diameter in the range of 0.1 to 100 μm [15–17]. The presence of these particles results in severe erosion of rotor blades and aerodynamic disturbances to the main flow path. The important parameters related to particles' trajectories and erosion phenomena are the diameter and speed. As such, measurements providing this information would have a substantial contribution towards improving the efficiency and safety of operation for conventional steam turbine power plants.

Researchers have produced a significant number of papers on turbomachinery applications that have developed different probe types to measure droplets' size and concentration in the stationary frame of a rotating machine. In this area, some of the first attempts were made by Walters *et al* [18] and Tatsuno *et al* [19]. Tatsuno *et al* developed an optical fiber probe to measure water droplets in a steam turbine using the forward scattering method. The probe tip diameter was 20 mm and the detectable droplet size ranged from 0.1 to 5 μm. In measurements performed in a 10 MW steam turbine they reported droplet diameters between 0.2 μm and 1.0 μm at the exit of the last stage. Young *et al* [15] measured coarse water flow rates in the last stage of a steam turbine using a custom designed water absorbent probe. Walters [20] describes a light extinction probe, which uses a xenon lamp and spectrophotometer to measure the spectral transmission of wet steam. The probe diameter is 25.4 mm and the spectral range of the system is 300 to 1100 nm, resolving droplet diameters 0.2 up to 1 μm. The light extinction method is also used in references [21, 22] for particle measurements mainly in steam turbines, in this case for liquid droplets with diameters of up to 10 μm. The probe tip diameters are limited to 20 mm. A different approach for fine droplet sizing ($D_d < 10$ μm) was proposed by Kercel *et al* [23]. They developed an optical system using a multiple-line argon laser in order to measure the size and velocity of water droplets in the last stage of an LP turbine without perturbing the flow. By splitting the laser beam into two through a converging lens, an interference fringe pattern is created forming the probe's measurement sample volume. The observing lenses collect light in the backscatter region through a single view port in the machine casing. In their results, Kercel *et al* report droplet diameters of up to 3.6 μm without specifying the exact measurement location in the machine or at the operating point. A number of recent developments have led to a combination of optical and pneumatic probes within one system for droplet measurements in steam turbines. These probes combine a pneumatic part for time-averaged pressure measurements and an optical part for wetness fraction measurements in steam turbines. Schatz *et al* [24] also developed this type of probe with a tip diameter of 10 mm, which combines the light extinction technique as well a pneumatic probe in the same tip. The tip of the probe has a wedge geometry to measure the time-averaged total and static pressure independent of Reynolds number. In addition, this probe incorporates two pressure taps in order to cover the wide range of pitch angles encountered in the flow in the last stages of LP turbines. As has been described so far, the majority of the developed probes for turbomachine applications have a minimum tip diameter of 10 mm and a detectable droplet size of up to 10 μm, and mainly implement time averaging techniques such as light extinction. Cai *et al* [17]

developed an integrated probe system for coarse water droplet measurements up to 400 μm in diameter. Their system consists of a fine droplet measurement subsystem that uses the light extinction technique and coarse droplet measurement subsystem using the forward light scattering technique. The tip diameter is 20 mm and it incorporates a 4-hole pneumatic probe part for the time averaged flow field measurements. In their results at the last stage of a steam turbine the droplet trajectories and speed under various operating conditions are presented. Xueliang *et al*'s noteworthy work [25] on probe development for coarse droplet measurements with imaging technique should also be mentioned. In this report the authors describe the development of a video-probe system capable of taking images of coarse water droplets ($D_d > 10$ μm) in order to measure their diameter and velocity. The probe is calibrated using standard monodispersed glass beads of up to 77.2 um in diameter as well as in spray environment with a known concentration and diameter. The main drawbacks of the last two approaches are the relatively large size of the probe tip ($D_p > 20$ mm) and the low measurement bandwidth on the aerodynamic part constraining the technique to time-averaged measurements.

As described in the previous paragraph, it is clear that the presence of coarse particles in the flow path of gas and LP steam turbines can result in undesirable engine operation. In order to improve engine efficiency and reliability, the flow mechanisms that dominate particle motion need to be understood and correlated to the main engine's operating flow field. The current paper presents the development of a novel fast response optical probe for particle measurements (FRAP-OB) developed in the Laboratory for Energy Conversion at the ETH Zurich. The work is focused on droplet measurements in steam turbines and the proof of concept of the probe was done with droplet measurements downstream of the stator in an axial turbine test facility (LISA) for two different operating conditions. In a latter step the probe was tested in a LP steam turbine facility and this work is described in [26].

2. Optical backscatter probe

2.1. General design requirements and operating principles

This section presents the requirements this probe should fulfill. According to the literature review the need for droplet measurements is focused in the range from 20 μm to maximum 120 μm in diameter. Therefore the new measurement technique should provide diameter and speed measurements of polydispersed coarse water droplets in that particular range. The probe should be able to use standard pneumatic probe access holes that are usually equipped with a guide pipe from the outer casing to the flow path. A typical diameter range for these access holes is 8 to 15 mm, therefore this constraint leads to a probe geometry which should be a simple single cylindrical shaft. The probe measurement volume should be minimized in order to resolve the droplets' size and speed distributions across the secondary flow structures present at the endwalls or in the blades' wake. The droplets' trajectories are triggered by the rotor blade-passing period and can

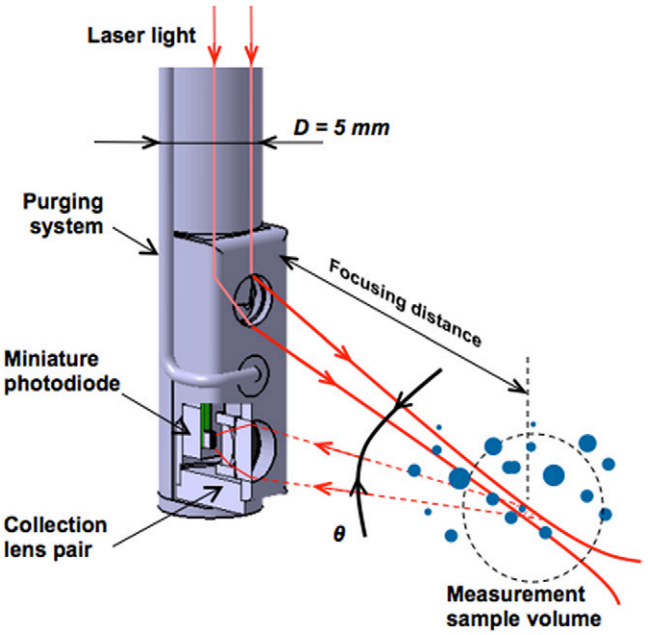

Figure 1. Operating principle schematic of the optical backscatter probe.

be exposed to flow velocities as high as 300 m s^{-1}, which sets the measurement bandwidth requirements to several tenths of MHz.

In general, the FRAP-OB probe presented in the current paper is a single-particle instrument that measures the light scattered from a droplet passing through an open path focused laser beam. The scattered light from the individual droplet is collected with optics over a given range of angles by a photodiode and converted to a digital signal, which is then related to a droplet size by applying the calibration curve. An assembly with optics focuses the beam three probe diameters from the probe surface. The principal reason for this is to avoid the probe disturbing the droplets' path when it is inserted into the machine. When a droplet crosses the measurement sample volume (focused area), light is scattered in all directions and a pair of lenses collects light in the backscatter region as shown in figure 1. The backscattered light is then focused in a miniature photodiode and the signal is transmitted via the electrical circuit to the acquisition equipment. In order to maintain the optics clean from any water contamination and beam deflection as the light exits the probe tip, an active purging system is installed. This provides pressurized air injected radially on the surfaces of the two lenses as presented in figure 1. The purging flow is attached to the surface of the windows so as to minimize any interaction with the surrounding flow field.

2.1.1. Optimal light scattering collection angle. Mie simulations were performed with the MiePlot v4.2 code [27] in order to identify the optimum backscatter solid angle. As depicted in figure 2, in the current simulations a Gaussian beam with light intensity I_o illuminates a water droplet. The droplet scatters light with intensity I in all directions and creates a scattering pattern. Figure 2 presents the scattering pattern from 0°, showing forward scattering (i.e. in the original light direction) of up to 180°, which implies back-scattering (i.e. back

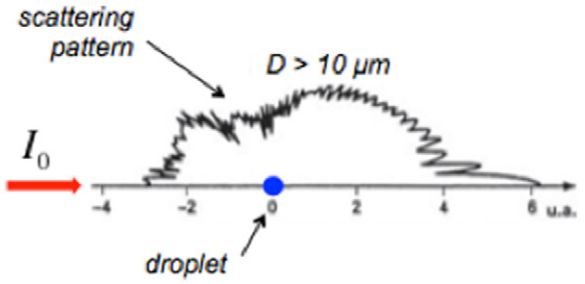

Figure 2. Mie simulations schematic.

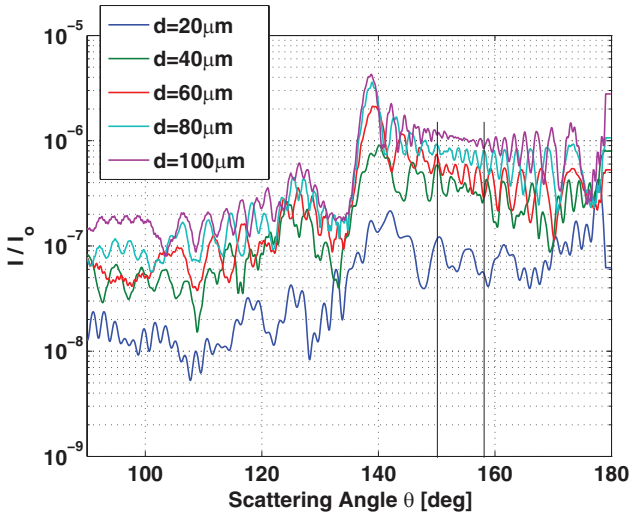

Figure 3. Mie calculation of scattering intensity by water droplet ($m = 1.332 + 1.53 \cdot 10^{-8}i$) for unpolarized red light ($\lambda = 0.632$ μm) for diameters $d = 20$, 40, 60, 80 and 100 μm.

towards the source of the light). For the case of a water droplet, the shape of this pattern depends on the droplet diameter and the incident wavelength, in this case 632 nm.

Figure 3 shows the scattered light intensity for various droplet diameters as a function of the scattering angle θ, from 90° to 180°, out of the Mie simulations as depicted in figure 2. The scattered light intensity I is non-dimensionalized over the incident light intensity I_o and plotted on a logarithmic scale on the y-axis. As shown in figure 3, the scattered light in the backscatter region between 138° and 160° shows a high sensitivity over the diameter range of interest. In order to fulfill the requirement of the focusing distance, 15 mm away from the probe surface, and at the same time increase the backscattered light sensitivity to the maximum possible, the collecting angle of the probe in the backscatter region was chosen to be between 150° and 158°. In this backscatter region the scattered light by a droplet shows a clear sensitivity to the scattered light intensity with increasing droplet diameter.

2.1.2. Sample volume. As presented in figure 1, the intersection of the focused beam with the scattered light collecting optics creates a well-defined sample volume in which a single particle scatters light when crossing it. The light is then recorded by the photodiode and converted into droplet diameter and speed using the calibration data as described

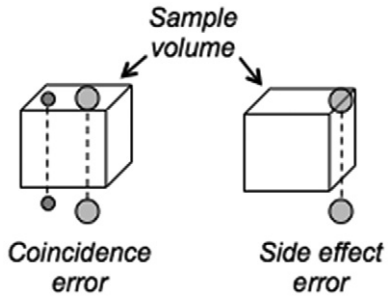

Figure 4. Representation of coincidence and side effect error.

in section 3. The geometrical characteristics of the measurement volume are a crucial factor in the design of an *in situ* particle instrument since the probe has to operate in a polydispersed droplet laden flow with unknown particle trajectories and concentrations. As described in [6, 28, 29] two types of errors may occur. The main two uncertainties related to the sample volume geometry are the coincidence and the side effect errors. Coincidence errors arise from the fact that more than one droplet crosses the sample volume at the same time. This type of error primarily depends on the droplets' concentration in the flowfield and it increases as the droplets' concentration increases. The side effect error is caused when a droplet partially crosses the sample volume. In this case the droplet is partially illuminated by the focused beam and therefore the recorded light signal is reduced, resulting in a fault size of the real droplet diameter. This error is mainly affected by the size of the droplet in the flow path relative to the size of the sample volume and large droplets relative to the sample volume are most prone to this type of error. A schematic of coincidence and side effect errors is presented in figure 4.

In addition to the coincidence and side effect errors there is an additional error due to light extinction of the laser beam. The beam light extinction occurs first when the laser light travels from the probe surface to the focusing point at the location of the sample volume and further light extinction occurs when the light is scattered from a droplet back to the photodiode. In order to select the optical components for the design of the sample volume size, the development was based on the extreme conditions found in the last stage of a typical low-pressure steam turbine. In order to maximize the power output of the steam turbines, the enthalpy difference between the inlet and exit of the machine has to be kept as high as possible. Therefore the steam is expanded to below the saturation conditions and the last stages operate under wet steam flow conditions. Depending on the operating condition and the backpressure of the turbine the wetness mass fraction is found to be in the range between 3–8%. The condensed water environment consists of very small droplets in the submicron range as well as coarse droplets of up to 100 μm in diameter [30, 31]. Nevertheless, the small droplets in the range of 0.1 to 1 μm contribute most to the concentration of the condensed environment. As described in [32], one way to calculate the droplet concentration is to use the specific volume of saturated vapor and liquid together with the wetness mass fraction. The concentration is a function of the droplet diameter

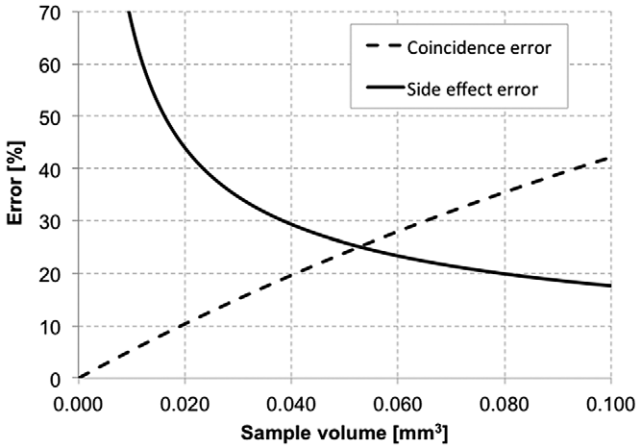

Figure 5. Calculated of maximum error due to coincidence and side effect.

and decreases as the droplet diameter increases. Using the analytical calculation of [32], the result for the average droplet diameter of 5 μm is about 10^{12} droplets m^{-3}. On the other hand, real measurements with optical extinction probes presented in [33, 34] report a concentration of 10^{13} droplets m^{-3} for a droplet diameter distribution of 1 μm. However, a recent study by Korolev *et al* [35] demonstrates the drawback of the extinction technique to underestimate the turbidity on the presence of coarse droplets ($D_d > 10$ μm). This implies that the real droplet distribution is shifted towards larger droplet sizes and therefore the actual concentration is overestimated. As a result, the new optical backscatter probe used a concentration of 10^{12} droplets m^{-3} for all calculations. The beam light extinction was calculated using the Beer–Lambert law as described in equation (1). When light with initial intensity I_o passes through an absorbing and scattering medium, in this case the droplets, the intensity decreases along its path L. Thus, the transmitted light I that reaches the control volume has a lower intensity, which is a function of the distance L and turbidity τ.

$$I = I_o e^{-\tau \cdot L} \tag{1}$$

The turbidity can be calculated using equation (2) assuming a droplet distribution of N(D) and applying the extinction coefficient E for the water medium.

$$\tau = \int_0^\infty \frac{\pi}{4} D^2 N(D) E_{(D,\lambda,m)} \mathrm{dD} \tag{2}$$

The reduction of incidence light intensity from I_o to I results in a proportional decrease of the calibration curve. As a consequence, the error in droplet diameter (due to light extinction) of the new probe is below 5% when measurements take place in an environment where the concentration is equal or lower than 10^{12} droplets m^{-3}.

The coincidence and side effect errors were calculated as described by Lance *et al* in [6] and Avellan *et al* in [28] respectively. For the coincidence error, a Poisson probability distribution of droplet interarrival passing times is used to calculate the probability of more than one droplet crossing the sample volume at the same time. In the probability distribution function the droplet concentration, speed and residence time in the sample volume are used. The side effect error uses the reduced scattered light function when a droplet partially crosses the sample volume. In this calculation the concentration and the apparent diameter cover factors are used. The resulted errors as a function of the sample volume size are depicted in figure 5. As expected, the coincidence error increases when the sample volume increases, since the probability of having more than one droplet at the same time in the sample volume increases. On the other hand the probability of a droplet partially crossing the sample volume is reduced as the sample volume is increased.

As presented in figure 5 there is an optimum volume for this particular concentration (10^{12} droplets m^{-3}), which corresponds to the minimum of the sum of the two error curves. This is in the range of 0.035 mm^3 resulting in 30% and 18% of the side effect and concidence error in diameter respectevely. In order to reduce the sources of these two errors, the sample volume of the optical backscatter probe was chosen to be roughly 0.01 mm^3, minimizing the coincidence error to below 5%. The side effect error is minimized through a correction routine which is described in section 3.2 (Correction for side effect error).

2.1.3. Photodiode selection. The principal requirement for the photodiode selection is the minimum response time. A sensor with a miniature size is favorable in order to keep the size of the probe as small as possible and minimize the distortion of the flow field around the probe tip. Since particles inside turbomachines can travel up to 300 m s^{-1}, a high speed PIN photodiode with 0.25 mm^2 square active area was chosen. The responsivity at $\lambda = 632$ nm is 0.49 A/W and has a maximum dark current of 0.1 nA which allows very low noise levels in the range of $\pm$0.5 mV after amplification on the raw data. The rising time of this silicon miniature sensor is 0.4 ns and is electricaly connected to a flexprint with gold wire bond completing the electrical circuit of the fast response optical backscatter probe.

2.2. Dynamic response

Since the selected photodiode has a very high bandwidth in the range of 3 GHz the dynamic response of the probe signal depends on the time response characteristics of the probe's signal conditioning unit that is equipped with the high-speed operational amplifier. When a droplet is crossing the measurement sample volume of the probe, the generated scattered signal is a typical Gaussian curve. For the current studies the probe was exposed to flow velocities of a maximum in the range of Ma = 0.5 (170 m s^{-1}). This requires a minimum bandwidth of 30 MHz in order to collect at least 10 measurement points for each crossing droplet to describe the generated Gaussian curve. As shown in figure 6, in order to achieve this bandwidth, the maximum allowable amplification is roughly 30 dB. This implies, with the current electronics, the probe is capable of detecting any droplet that travels with a speed up to 170 m s^{-1} without any measurement bandwidth limitation.

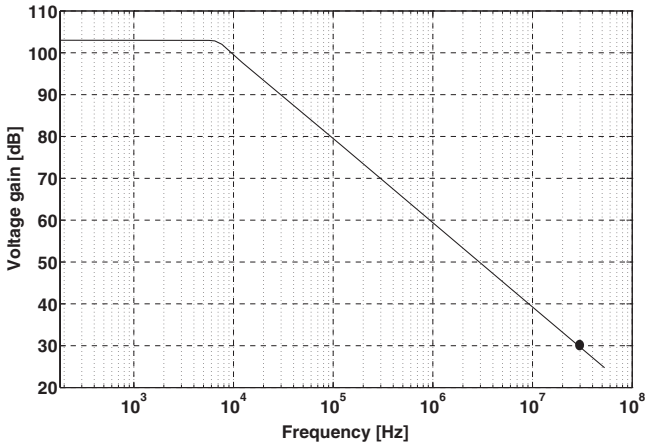

Figure 6. Amplitude response of the optical backscatter probe out of simulations.

Figure 7. The optical backscatter probe tip.

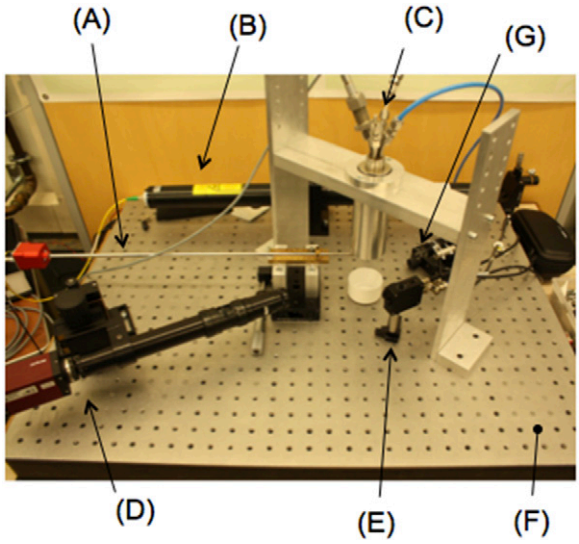

Figure 8. Monodispersed calibration system schematic A: Probe, B: He-Ne Laser, C: Droplet generator, D: Reference camera, E: Droplet monitor diode, F: Optical table, G: Strobe light.

2.3. The FRAP-OB probe

The newly developed FRAP-OB probe is presented in figure 7. It has a tip diameter of 5 mm and maximum operating temperature up to 120 °C. The distance between the collecting pair lenses and the optical window where the light source exits the probe tip is about 7 mm. A purging system is installed between the two optical components and pressurized air on the flat surface of the probe keeps the two windows clean from any water contamination. The purging system is controlled through the measurement computer and it is only activated for roughly 0.2 s before each measurement. The control and monitoring system of the probe consists of an integrated signal conditioner, a multi-axis probe traversing system and a laboratory PC that is equipped with an acquisition card with high sampling rate capable of acquiring signals up to 250 MHz. The optical fiber at the end of the probe is connected with a 28 mW He-Ne laser that is attached to the traversing system. Two channels are recorded during measurements, one is the photodiode signal from the probe and the second is the rotational speed of the machine. The two records are made in order to rephase the measurements with respect to the rotor blade passing period.

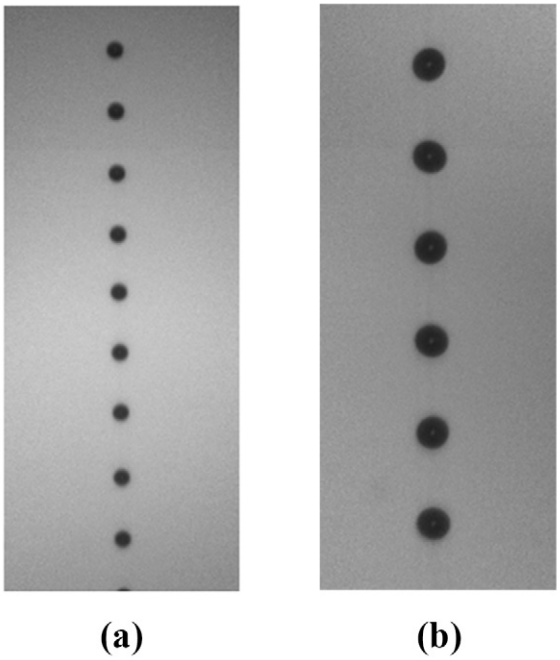

Figure 9. Raw images from reference camera for 60 μm droplet diameter (a) and 105 μm droplet diameter (b).

3. Probe calibration

The optical backscatter probe is calibrated using a monodispersed calibration facility. A schematic of the calibration system is shown in figure 8. The probe (A) is mounted on a 2D-XY translation stage system enabling movements on the surface of the optical table (F) with an accuracy of 5 μm. The light is generated with the 28 mW He-Ne laser (B) and guided through the probe's optical fiber into the probe tip. The probe calibration is performed using an in-house droplet generator (C) developed by Rollinger *et al* [36]. The monodispersed droplet generation in the kHz range is based on the Rayleigh breakup jet. A modular design, based on cartridges, which are composed of the water reservoir and the dispensing nozzle,

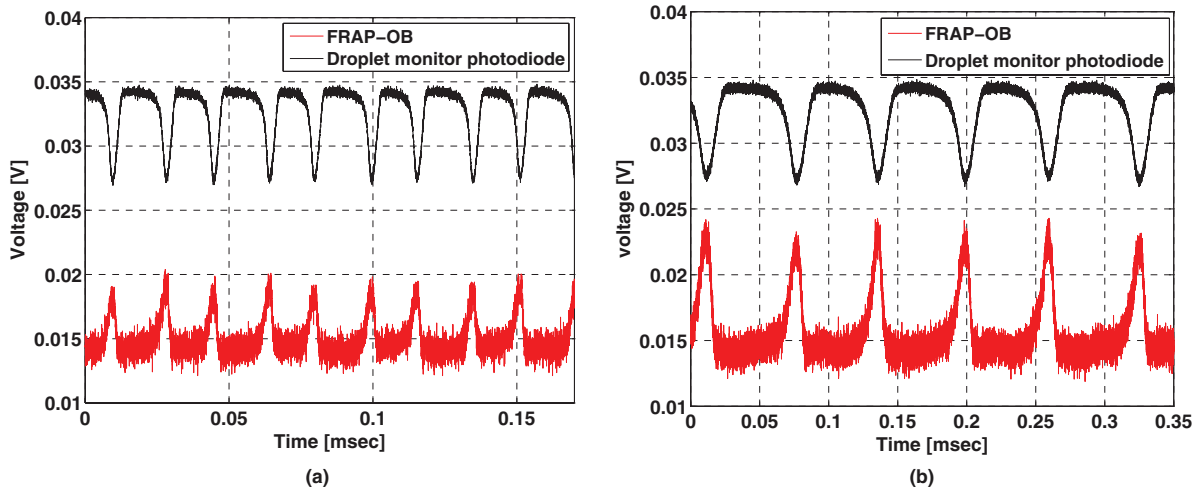

Figure 10. Probe and monitor photodiode raw signals during calibration for 60μm droplet diameter (a) and 105 μm droplet diameter (b).

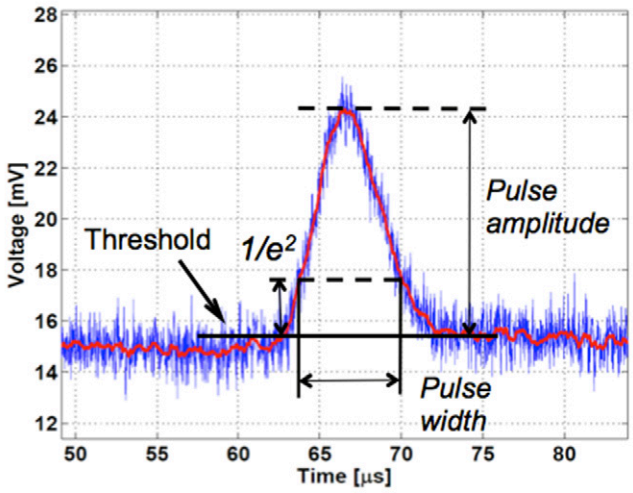

Figure 11. Single droplet measured parameters after calibration.

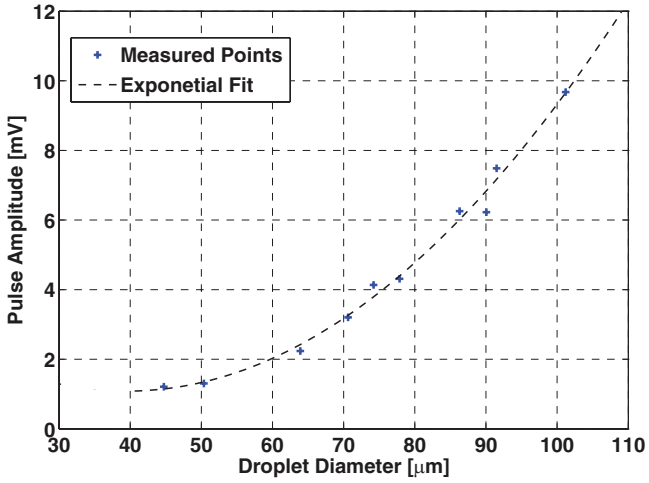

Figure 12. Calibration curve of the optical backscatter probe with water droplets obtained from the droplet generator.

is capable of producing water droplets from 40 to 100 μm in diameter with a stability of ± 2 μm. Water droplets are generated continuously with a frequency and air-backpressure set

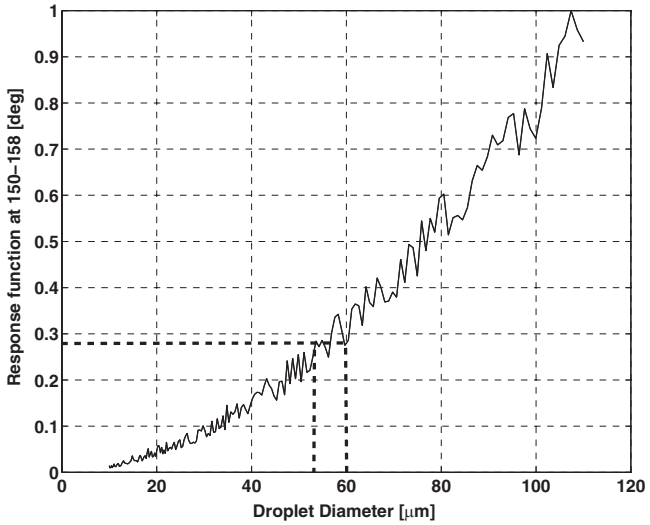

Figure 13. Theoretical response function in the backscatter region for water calculated from the Mie theory.

by the user. Depending on the tuning parameters, the droplets' velocity range is from 4 to 12 m s^{-1}. The performance of the droplet generator device is monitored continuously with a commercial fast response photodiode PDA 100 A, represented as (E) in figure 8, in order to achieve uniform and equally spaced droplets. The monitor photodiode is positioned in the probe's exit light direction; therefore the droplets' signature creates a forward scattering signal. A neutral density filter is attached to the photodiode in order to reduce the intensity of the forward scattered signal.

For independent referencing of the droplet diameter the shadow imaging technique is utilized. As shown in figure 8, the droplets are imaged with a high-resolution camera (D). The camera's resolution and pixel size is 2452 $\times$ 2054 and 3.45μm respectively, it has 5 $\times$ maximum optical magnification and is triggered by the strobe light (G). In order to acquire high quality sharp images of the droplets, the camera is mounted on a 3D-XYZ translation stage system. The shadow imaging technique is used to produce pictures of the generated water droplets. In a second step, the obtained pictures

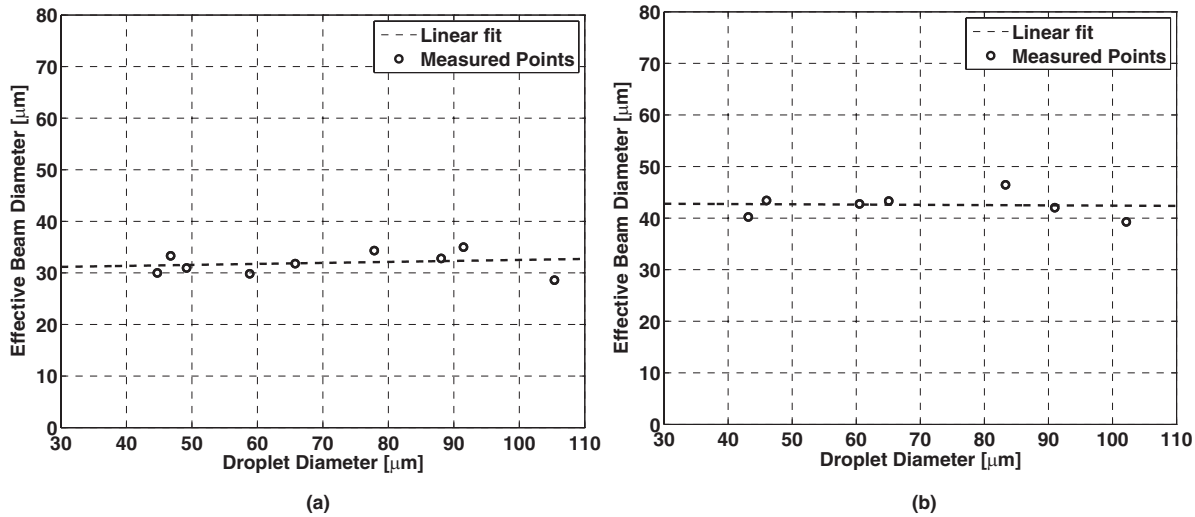

Figure 14. Effective beam diameter as a function of droplet diameter for calibration tilting angle 0° (a) and tilting angle 49° (b).

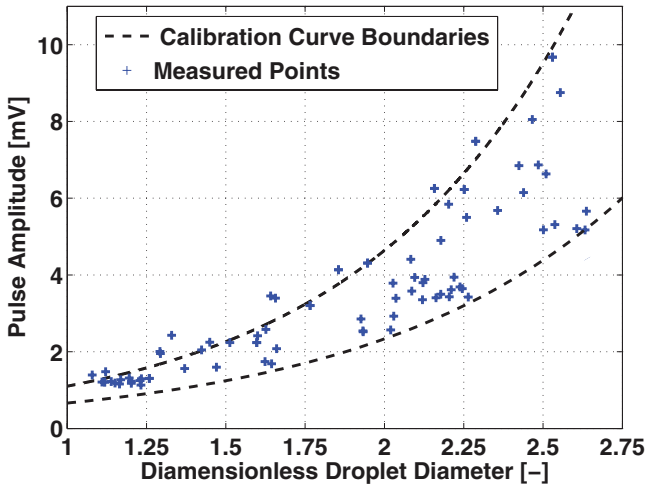

Figure 15. Probe's output signal (mapping) when droplets are partially crossing the sample volume.

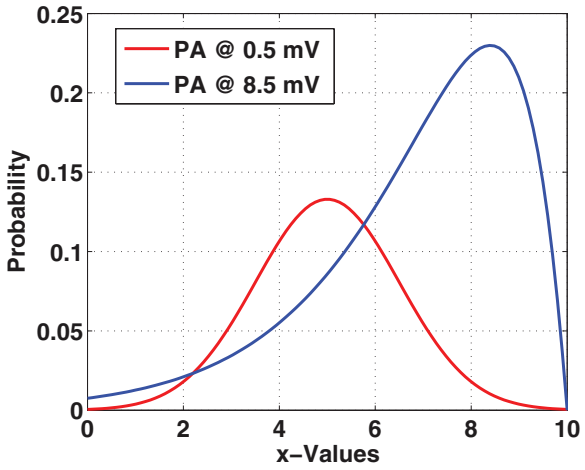

Figure 16. Droplet's diameter probability distribution function related to the probe minimum signal amplitude (PA = 0.5 mV) and maximum signal amplitude (PA = 8.5 mV).

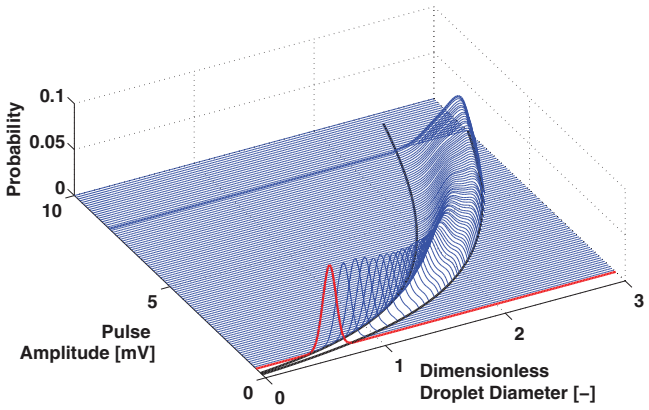

Figure 17. Probability distribution model for the calibrated range of the optical backscatter probe.

are analyzed in MATLAB environment to measure the droplet diameter. When using the maximum amplification factor, the accuracy of this technique results in an error of ±0.69 μm in diameter. The probe's voltage signal is correlated with the droplets' measured diameter in the last step of the post processing analysis.

Two raw images as they are captured with the reference camera when the droplet generator is in operation are shown as examples in figures 9(a) and (b). Both images have the same magnification factor (optical zoom 2x), which results in 1.725 μm pixel image resolution. In figure 9(a) the droplet generator was tuned to operate at 57 kHz, producing droplets with a diameter of 60 μm. In figure 9(b) the droplet generator was operating at 16 kHz and the size of the produced droplets is 105 μm. In order to achieve sufficient statistical data, multiple pictures were recorded and as consequence the droplet count exceeds 100.

The raw signals presented in figure 9 from the optical probe and the monitor photodiode are presented in figure 10 for the two droplet diameters. The data are acquired at a sampling rate of 62.5 MHz over a period of 8 ms with a resolution of 12 Bit. As shown in figure 10, the offset signal of the FRAP-OB probe (sensor's dark current) is 14.5 mV and the RMS noise is ±0.6 mV. The FRAP-OB signal has a rising slope since it

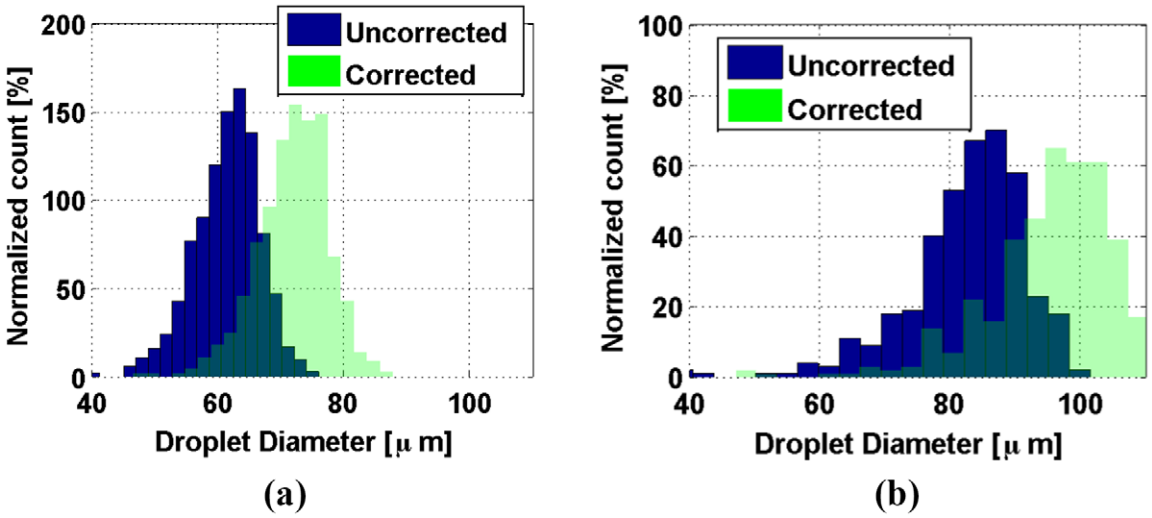

Figure 18. Correction example of small (a) and large (b) droplet distribution by applying the probability distribution model.

Table 1. Sources of uncertainty related to the calibration procedure.

	Parameters in the three regimes			
	low	mid	high	Units
Source of uncertainty	40–65	65–85	85–110	μm
Reference camera system	±0.43	±0.56	±0.56	μm
Uncertainty due to non monotonic behavior	±3.5	±4	±3	μm
He-Ne power laser drift stability	±2	±2	±2	%
Voltage measurement with DAQ system	±0.02	±0.02	±0.02	mV

Table 2. Sources of uncertainty from the measurements.

	Parameters in the three regimes			
	low	mid	high	Units
Source of uncertainty	40–65	65–85	85–110	μm
Calibration procedure	±4.1	±4.7	±3.5	μm
Coincidence error	±2.5	±2.3	±2	%
He-Ne power laser drift stability	±2	±2	±2	%
Voltage measurement with DAQ system	±0.02	±0.02	±0.02	mV
Overall uncertainty	±4.7	±5.4	±4.0	μm

collects backscattered light when a droplet travels through the sample volume. One can say that in this case the scattered light is 'reflected' and afterwards it is captured from the probe's photodiode. On the other hand, the signal from the monitor diode demonstrates a falling slope, since it collects forward scattered light and the droplet 'blocks' the light, when it crosses the sample volume. As shown in figures 10(a) and (b), the larger the droplet size the higher the backscattered light is. Therefore, in order to find the correlation between the droplet diameter and the probe's output signal, the droplet generator is tuned to produce various droplet sizes with a step of 10 μm and the respective pulse amplitude signals from the probe are compared.

For each individual droplet the two main parameters that are extracted are the pulse amplitude and the pulse width. Using the reference camera data, the pulse amplitude is correlated to the size of the droplet and the pulse width to the speed that the droplet travels. As presented in figure 11, the pulse amplitude is measured from a threshold value that is 3σ of the noise level and the pulse width is calculated at $1/e^2$ (13.53%) of the peak height.

The resulting calibration curve is presented in figure 12. The calibration curve correlates the maximum measured pulse amplitudes to the respective droplets' diameters obtained using the reference camera. The droplets always cross the two intersecting light paths (laser beam and observer light path, (figure 1) perpendicularly, which implies that the droplet jet and the probe axis are perpendicular to each other. The response of the probe as a function of droplet size exhibits some oscillations, which result in a correlation factor of $R^2 = 0.957$ between the exponential fit and the calibration data. As presented in figure 13, the theoretical response of the backscattered light as a function of the water droplet diameter, calculated with the Mie theory, does not increase monotonically. Therefore the relatively poor correlation factor of the calibration curve fit is a direct consequence of the oscillatory behavior of backscattered light intensity as a function of droplet diameter. For instance, in figure 13 the dashed line shows an amplitude response signal that can correspond to two different droplet diameters. Similar trends from simulations or experiments are reported in [6, 8, 37]. The non-monotonic behavior of the theoretical Mie scattering response leads on average to ±3 μm uncertainty related to the calibration model exponential curve fit.

The measurements in the turbine research facility (LISA) presented in this paper were conducted at different droplet entry angles compared to the calibration curve. The main droplet direction in the flow path was 49 deg instead of

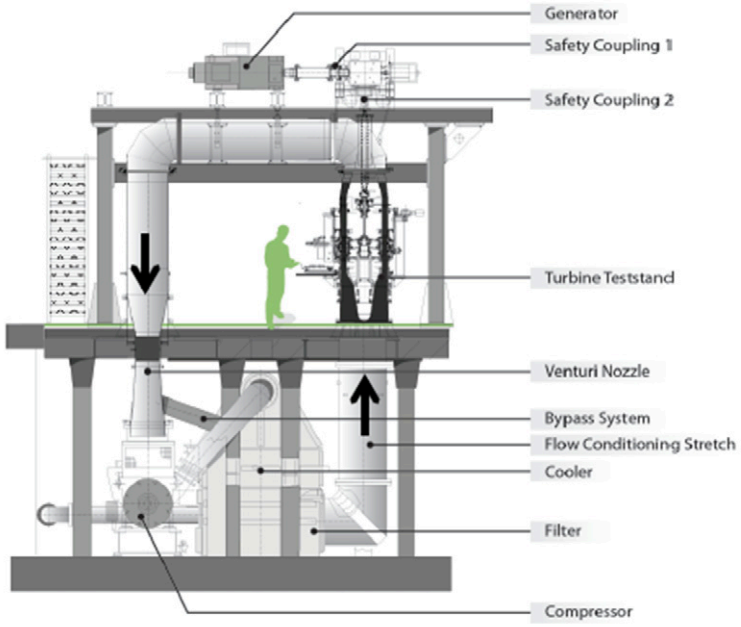

Figure 19. Schematic of LISA turbine test facility.

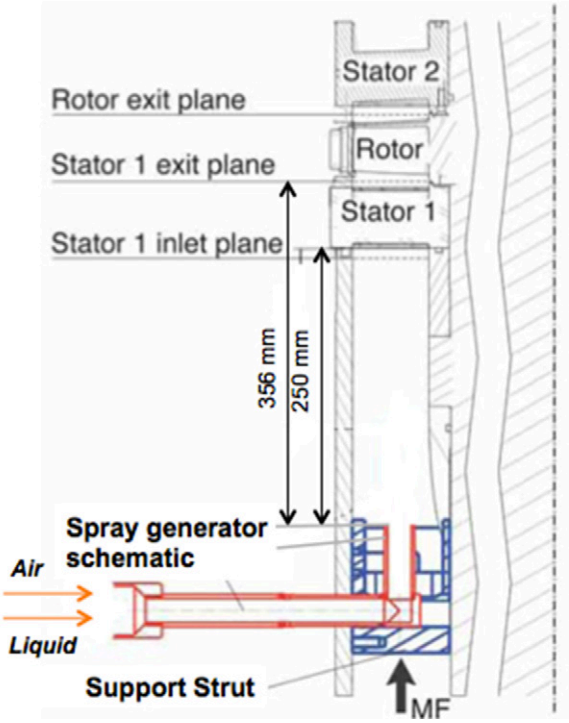

Figure 20. Cross section of the test segment (Turbine Teststand).

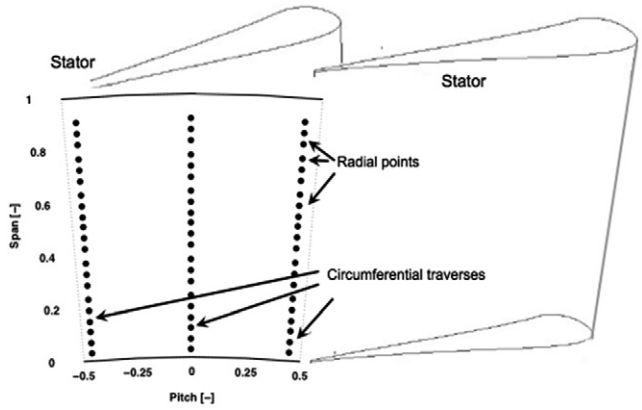

Figure 21. Measurement grid schematic at the experiments performed in LISA test rig. The observer looks upstream. The measurement grid consists of 21 × 41 points equally spaced in the radial and circumferential direction, and covers one full stator pitch from 5% to 95% span.

Table 3. Operating conditions and geometrical characteristics.

	Design point	Part load
Rotor speed [RPM]	2700	2700
Rotor/stator blades	54/36	54/36
Rotor blade passing freq [Hz]	2430	2430
Pressure ratio 1.5-Stage,tot-st	1.65	1.33
Turbine entry temperature [°C]	55	55
Total inlet pres. [bar abs norm]	1.4	1.2
Stator 1 exit average mach number	0.52	0.42
Stator 1 exit flow angle [deg]	73.1	72.8
Mass flow [kg s^{-1}]	12.13	8.4
Shaft power [kW]	288	132
Hub/tip diam.[mm]	660/800	660/800

the 90 deg that was described in this calibration procedure. Therefore additional sensitivity studies were performed in order to verify the validity of the probe results under various crossing paths of the water droplets. The discrepancies found between the different calibration curves are within the calibration uncertainty bandwidth of the optical backscatter probe and therefore for the droplet size measurements the

same calibration curve was applied for the 49 deg as well as for the 90 deg tilting angle.

3.1. Calibration for speed measurements

In order to be able to obtain the speed of the droplets in an unknown flowfield environment, a calibration procedure was performed with the same calibration set up as presented in figure 8. The velocity of the droplets was calculated from the images taken with the reference camera by multiplying the distance between the two consequent droplets with the droplet generation frequency equation (3),

$$V = L \times fg \tag{3}$$

Knowing the droplet speed and the pulse width (residence time, t_{res}) as depicted in figure 11, one can calculate the effective beam diameter, which is the laser beam diameter that a droplet 'sees' when it crosses the sample volume with equation (4),

$$D_{eff} = U \times t_{res} \tag{4}$$

This effective beam diameter is a function of the droplet diameter since the scattering surface of a large droplet is greater compared to a small one in the same location and of the sample volume. This trend is only valid when the laser beam diameter is completely symmetrical in all directions and therefore the scattered signal does not depend on the direction in which the droplets that will cross the sample volume are travelling. The result of the droplet calibration speed is shown in figures 14 (a) and (b) for the two calibration cases. Both cases show relatively low scatter around the mean value. In addition there is a small change on the linear curve fitting between the two cases. This small change on the slope can be attributed to the non-symmetrical shape of the laser beam diameter. Nevertheless, the results have shown that the effect on the entry angle of the droplet to the probe's sample volume can be neglected.

3.2. Correction for side effect error

In this section, the correction routine accounting for the side effect error is described. This error is responsible for the underestimation of droplet size when the droplet crosses the sample volume partially. The calibration set up allows for the quantification of this error and in a second step, the development of the correction algorithm. The calibration curve presented in figure 12 is obtained using monodispersed water droplets ranging from 40 to 110 μm in diameter with step increases of about 10 μm. In order to assess the magnitude of the underestimation in droplet size, the response to the optical backscatter probe was mapped by moving the probe relative to the calibration system using high precision (5 μm) linear translation stages. The maximum light scattering intensity output of the probe is used in the calibration curve depicted in figure 12. In this case the droplets cross the sample volume at its center. By moving the probe in the *XY* plane perpendicularly to the droplet train, the response output across the sample volume was mapped for each droplet diameter used in the calibration

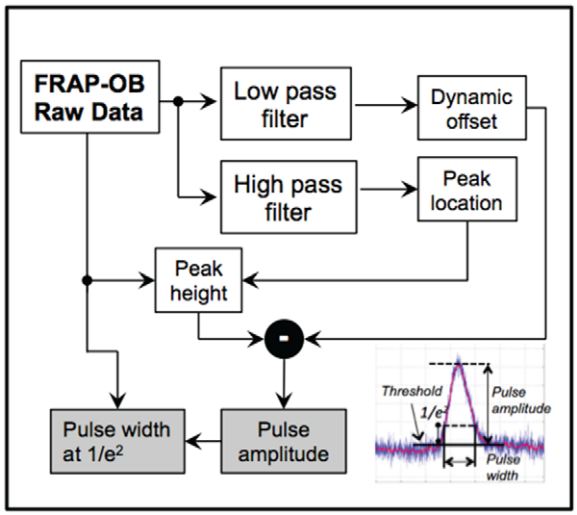

Figure 22. Flow chart of the post processing algorithm.

of the probe. The results are shown in figure 15, which illustrates that for the same droplet size the probe output varies between a minimum and maximum value (two dashed lines). In the same plot the droplet diameter is non- dimensionalized with the beam diameter. Since the side effect error depends on the droplet size as described above, the deviation of the two curves for large droplets is higher in comparison to the small droplets. In other words, the probability of small droplets (up to 50 μm) partially crossing the sample volume is reduced significantly but the probability of large droplets (range of 100 μm) partially crossing the sample volume is increased for the current design of the FRAP-OB probe.

As a result, it is evident in figure 15 that due to side effect error the response output (pulse amplitude) of the probe for a constant voltage results in a certain range of droplet diameters. As depicted in figure 15, this range is set by the two boundaries of the dashed lines. In order to correct this behavior, a probability distribution function was modeled for the whole spectrum of the droplet diameters from 40 μm to 110 μm. Based on the measured scatter of the calibration data described in figure 15, the probability distributions for the small and large droplets were identified to follow a normal (red) and a skewed normal (blue) distribution as shown in figure 16.

For the current correction model, an output signal that corresponds to small droplet sizes will be modeled with a normal distribution that has its boundaries between the two dashed lines in figure 15. On the other hand, the output signal for the large droplet sizes will be modeled with a skewed distribution, as presented in figure 16, in order to account for the greater probability of the side effect error with increasing droplet diameter. All intermediate droplet diameters have probability distributions that will gradually vary from normal to normal skewed distribution. The resulting 3D probability distribution correction model is presented in figure 17.

Each measured droplet distribution is corrected by applying the probability distribution model to the measured distribution described above. The results are shown in figure 18(a) and (b), and as expected the correction model shifts the distributions

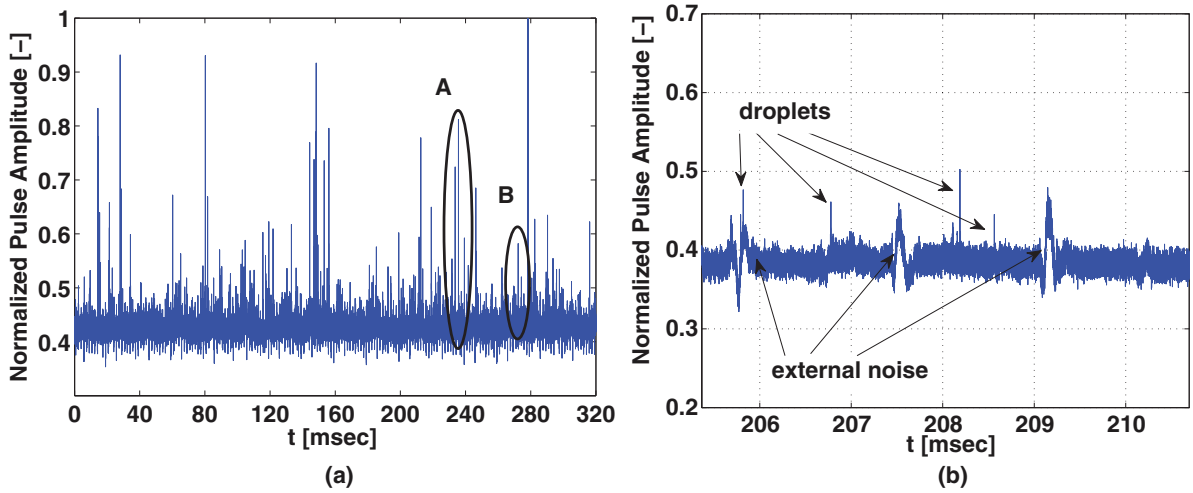

Figure 23. Single measurement point raw data file over 14 rotor revolutions (a) and the same raw file zoom in over 4 detected droplets (b).

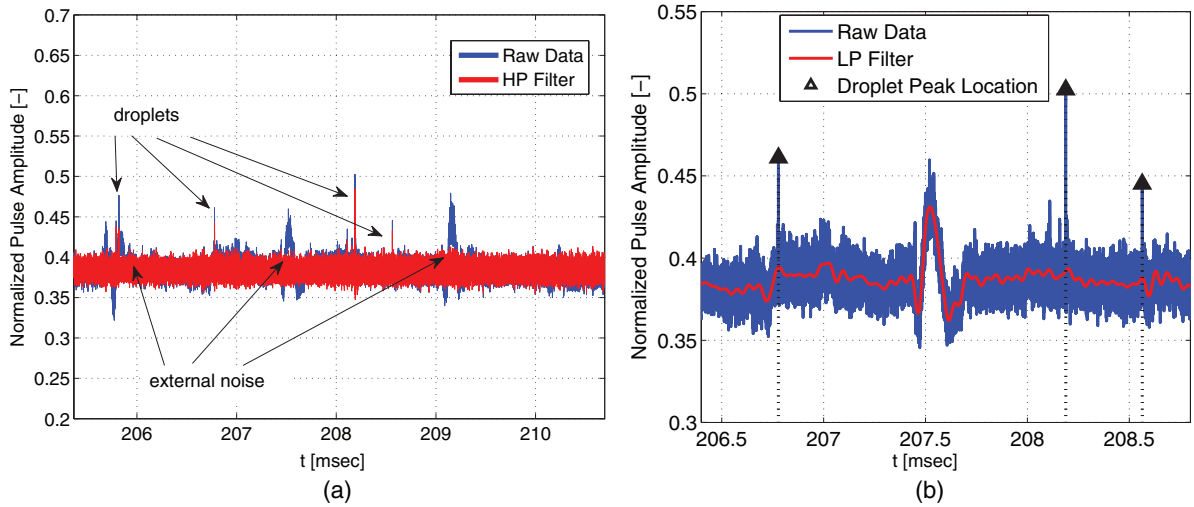

Figure 24. Utilization of high pass filter (a) and low pass filter (b) in raw data.

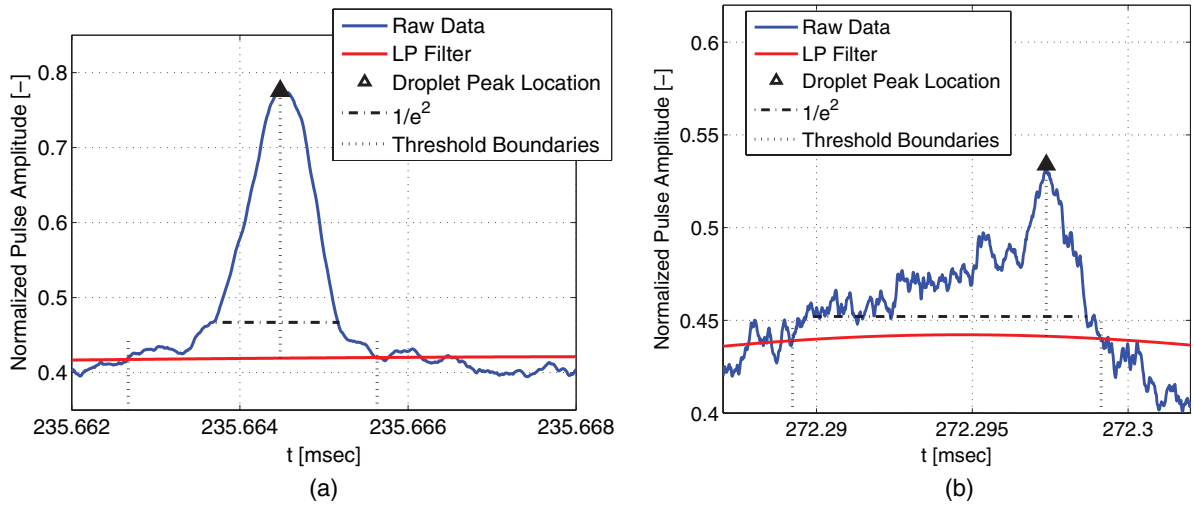

Figure 25. Zoom in a single valid droplet at time location A (a) and a non valid droplet at time location B (b).

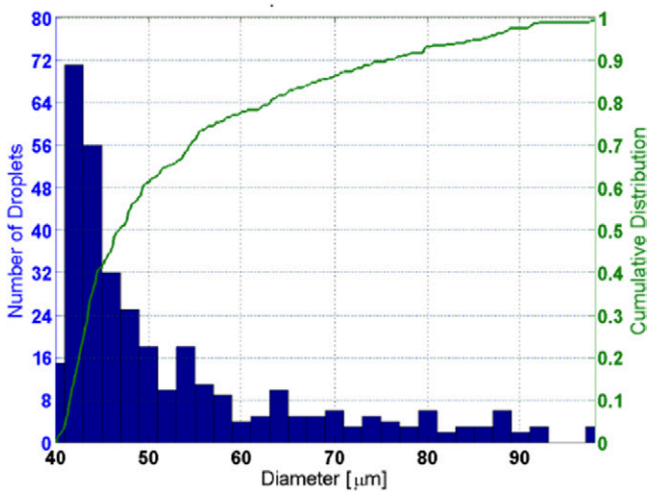

Figure 26. Single measurement point probe representation results. Voltage peak heights that fulfill the detection criteria are converted into droplet size and presented as a size distribution histogram.

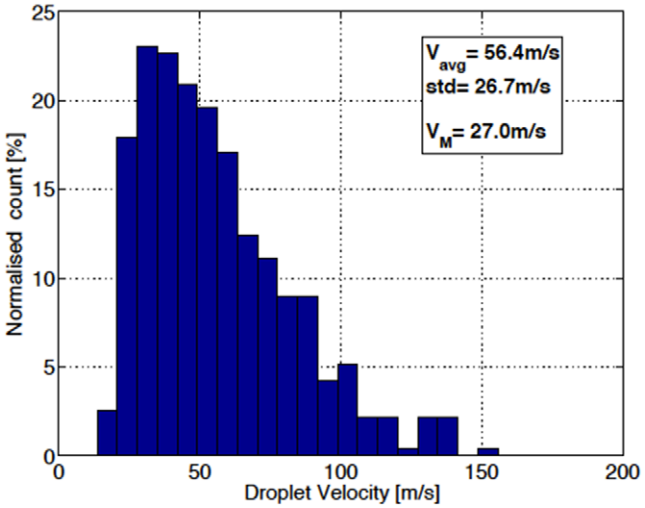

Figure 27. Single measurement point probe representation results. Voltage pulse widths that fulfill the detection criteria are converted into droplet velocity and presented as velocity distribution histogram.

towards larger droplet diameters in order to account for the side effect error. As presented in figure 18, in the case of small and large droplet distributions, the Sauter mean diameter has increased from 62 to 70 μm and from 80 to 93 μm respectively. The sample size for the distributions of figure 18(a) and (b) is 200 droplets.

4. Uncertainty analysis

In this section the sources of measurement errors related to the optical backscatter probe are identified and the resulting overall uncertainties in derived droplets' diameter and speed are calculated. The whole chain of uncertainty sources has been accounted for starting with the uncertainties resulting from the calibration references as well as the uncertainty sources related to the measurements. The resulting overall uncertainties are calculated using the Gaussian error propagation formula. The uncertainty calculation was performed using the guide to the expression of uncertainty in measurement (GUM) Workbench [38].

4.1. Calibration uncertainties

Since the sensitivity of the calibration model curve of the probe is not constant within the calibration range, the uncertainty analysis for the calibration procedure is divided into three regimes to better describe the uncertainties. These three ranges are from 40 to 65 μm, from 65 to 85 μm and from 85 to 110 μm. For each calibration range the uncertainty analysis is performed using the mean value in that particular regime. Table 1 lists the sources of uncertainties from the calibration procedure of the optical backscatter probe.

The uncertainty for the reference camera system is derived from the ratio of the minimum pixel size divided by the magnification factor (camera zoom). The second source of uncertainty is derived from the non-monotonic behavior of the light scattering from the droplet in the backscatter region. As shown in figure 13 and described in the corresponding paragraph, the theoretical response of the backscattered light as a function of the water droplet diameter does not increase monotonically. In order to have a model that describes this relationship monotonically, the fluctuations on the response signal have to be accounted for. Therefore, the uncertainty in droplet diameter from the model is ± 3.5 μm, ± 4 μm and ± 3 μm for the low, middle and high regime respectively. In addition, the power drift of the laser is included in the uncertainty chain analysis. This is $\pm 2\%$ over a period of 8 hrs and it corresponds to backscatter signal fluctuations during calibration. Last but not least, the uncertainty on the voltage measurement is set by the 12 Bit acquisition system used over an analogue input range of ± 100 mV, which provides a maximum signal voltage resolution of ± 0.02 mV and is constant for all regimes. Combining the above sources of uncertainties, the absolute error in diameter from the calibration procedure for the low, central and high regime is calculated to ± 4.1, ± 4.7 and ± 3.5 μm respectively.

4.2. Measurement uncertainties

In addition to the calibration uncertainties, the uncertainties during the measurements in the axial turbine test facility LISA are presented in the current paragraph. The main sources of uncertainties during measurements are the coincidence error as well as the laser drift stability as described above. The side effect error is not included in the current calculation since the correction model is applied in the post processing code to account for it. In addition, the resulting errors from the calibration procedure for the three distinct regions are included in the error propagation calculations for the measurements. The uncertainties from the measurements are presented in table 2 and the overall uncertainty of the probe for the three regimes is calculated to ± 4.7, ± 5.4 and ± 4.0 μm respectively. In the current measurement campaign the averaged droplet speed results are in the range of 40 to 50 m s^{-1}. The calculated uncertainty of the speed measurements is ± 2.3 m s^{-1}.

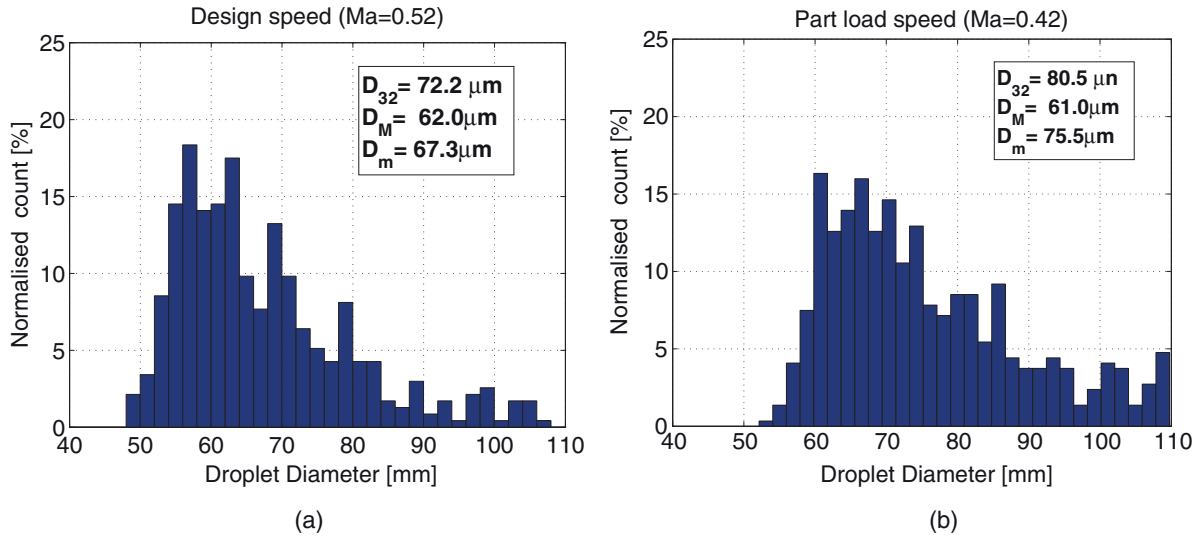

Figure 28. Size droplet distribution at mid spanwise location for design point and part load conditions at $x/c = 2\%$ downstream stator exit.

5. Application of the probe in the axial turbine facility 'LISA'

A set of measurements to demonstrate the capability of the optical backscatter probe was performed in the axial research turbine test facility 'LISA'. A schematic of the experimental test facility is shown in figure 19. For the present measurements, the facility was equipped with a 1.5 stage of an axial turbine that is described in Behr *et al* [39] The measurements were performed at a constant rotor speed of 2700 rpm, which corresponds to a rotor blade passing frequency of 2430 Hz. The measurements presented in the current work were made at 2% and 8% stator axial chord downstream of the stator's 1 trailing edge for two different operating conditions as depicted in figure 20. This implies that the FRAP-OB probe was inserted 356 mm downstream from the injector location between Stator 1 and Rotor. As shown in figure 21, the measurement grid is comprised of 21 points in the radial direction covering the stator span from 10% up to 90%. In the circumferential direction the measurement grid consists of 41 equally spaced traverses that cover one stator pitch (10 deg). The measurements were performed under a part load condition as well to investigate the droplet formation at reduced relative flow velocities. The operating parameters for the two measured conditions are summarized in table 3.

A custom-made water spray generator was installed 5 stator chords upstream of the test section. The current droplet generator is capable of generating a spray with droplet diameters from 1 to 200 μm covering one and a half stator passages and injecting droplets at mid-span location with a mass flow of 0.16 l/min. The spray generator was embedded in a support strut with a standard NACA 0012 profile to create an aerodynamic shape and minimize any interactions of the injector body with the generated water spray and flow field. Measurements were performed at the inlet plane as well as at the Stator 1 exit plane for the two different operating conditions. A schematic of the test section region with the custom-made droplet generator is shown in figure 20.

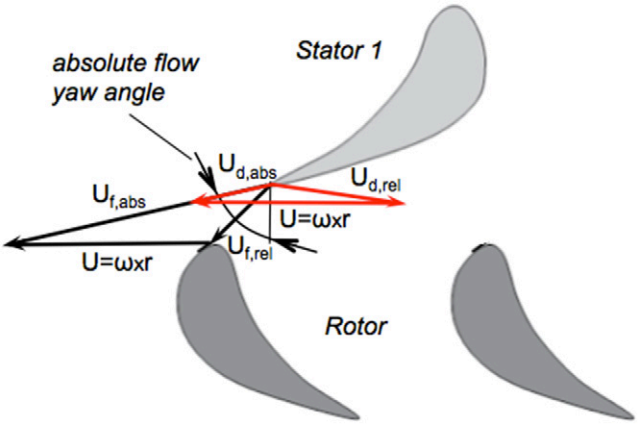

Figure 29. Velocity vectors' flow field (black) and droplets (red) at Stator 1 exit.

5.1. Single measurement point processing algorithm

For the novel measurement system a multi-step post-processing algorithm for droplet detection was developed. As mentioned previously, the FRAP-OB probe is a single particle detector. This implies that every droplet that crosses the sample volume of the probe (figure 1) will generate an output signal. The backscatter signal from small droplets is at least three to four orders of magnitude lower than the respective forward scattering signal, which leads to a relatively low signal-to-noise ratio for droplets in the lower diameter range. In addition, as mentioned previously, in order to detected droplets with high velocities, the probe is equipped with a high bandwidth amplifier. As a consequence, the probe signal collects noise from surrounding devices affecting the signal-to-noise ratio over a wide range of frequencies. A flow chart of the post-processing algorithm is presented in figure 22. The pulse amplitude and width are extracted from the raw data of the probe following the procedure described in the following paragraphs.

A typical raw data file downstream of Stator 1, around midspan, is shown in figure 23(a). Over a measurement time

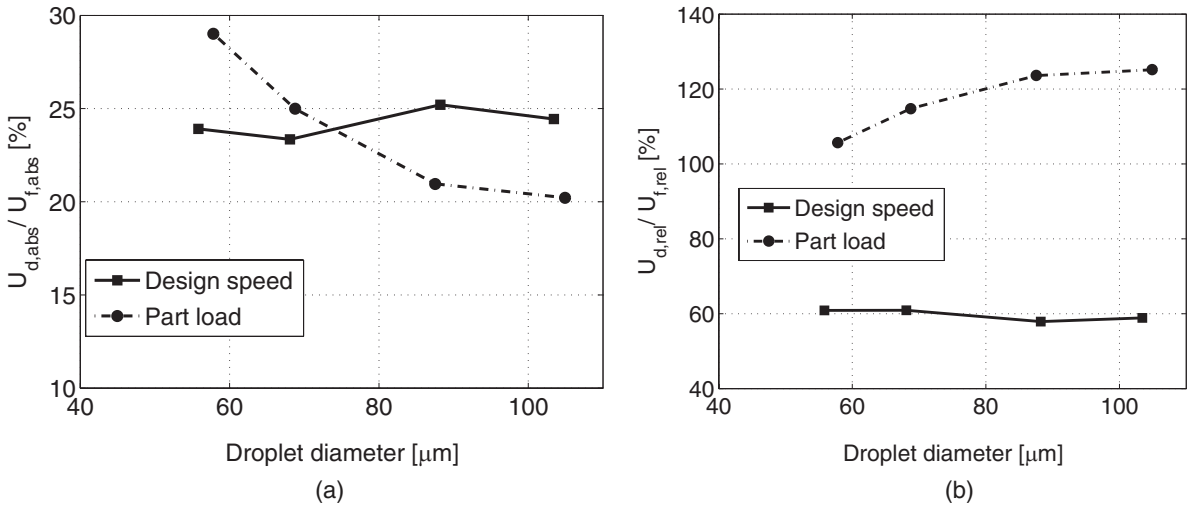

Figure 30. Absolute droplet velocity (a) and relative droplet velocity (b) at mid span region for design point and part load conditions at $x/c = 2\%$ downstream of stator exit.

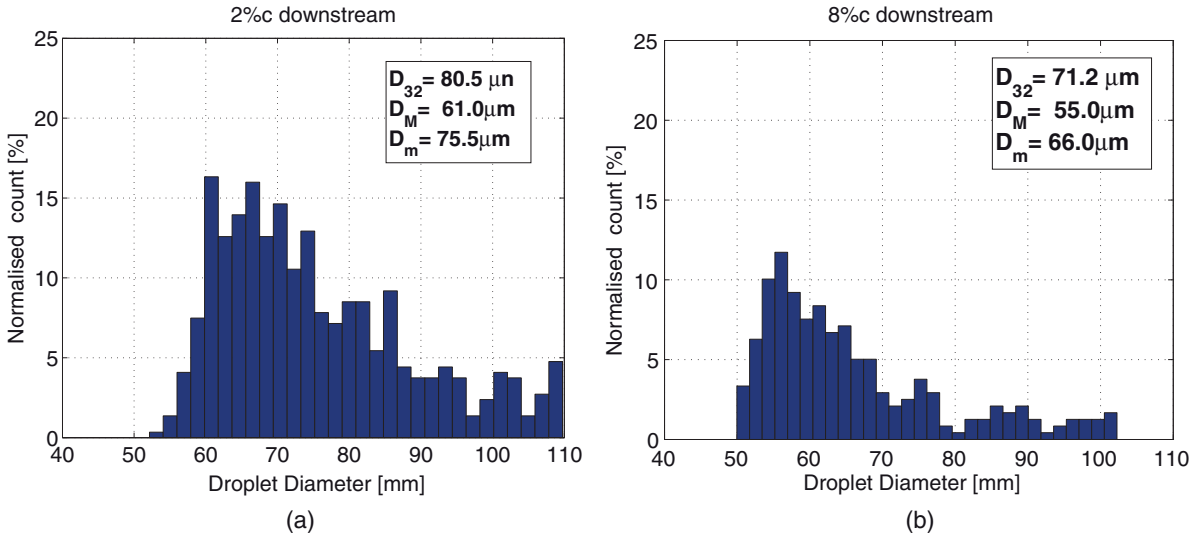

Figure 31. Size droplet distribution at mid spanwise location for part load condition at two locations downstream of the stator.

period of 320 ms the droplets appear as single vertical lines. Figure 23(b) shows the signal over a reduced time period of 6 ms and it illustrates that the detected droplets as well as external periodical noise signatures fall into the same amplitude response. In order to allow for accurate measurements and extend the lower droplet diameter detection range several signal-filtering and detection steps have to be applied as presented below.

The filtering steps include the utilization of a high pass filter to locate the droplets by filtering out low frequency external noise content while keeping fast droplets' signals content and the utilization of a low pass filter in a second step in order to get the dynamic ground signal of the probe (sensor's dark current) by keeping the external low frequency periodic noise.

Apply High Pass filter

- Calculate the mean value (μ) and the standard deviation (σ) of the ground noise of the signal
- Locate the droplets on the high pass filtered data as shown in figure 24(a). When the peak voltage is above the value of $\mu + 3\sigma$ from the ground noise the sample (time) of that peak is stored

Apply Low Pass filter:

- Get the dynamic ground signal of the probe that follows any external noise (figure 24(b))

Calculate the pulse amplitude of each droplet:

- Check on the raw data (figure 24(b)) the location (sample) where the droplets were recorded in the first step with the HP filter
- Calculate at that location the voltage difference between the peak and the dynamic ground signal obtained from the LP filter.

The dynamic ground signal is indicated as a red line in figure 24(b) and the droplets which have been tracked are highlighted in the same figure with a black triangle.

In the post-processing step the considered peaks are checked for reliability. There are several criteria that have

to be fulfilled in order to consider the measured signal as a valid droplet. The droplets that fulfill these criteria are marked with a triangle at their signal peak height. A valid detected droplet at time location A (figure 23(a)) is presented in figure 25(a). The signal is a symmetrical Gaussian profile as recorded during the calibration procedure implying a valid droplet. For each valid droplet the pulse amplitude is measured as well as the pulse width at $1/e^2$ of the total peak height. The peak height in figure 25(b) that shows the detected droplet at time location B (figure 23(a)) is not valid. The signal pattern reveals that this particular droplet is not spherical since the shape of the signal does not match with the calibrated one. Therefore in the last step of the data processing this droplet is not counted. The detection criteria of the post-processing algorithm are mainly related to shape, size and signal to noise ratio of the recorded signals. In this measurement campaign the data was acquired with a sampling rate of 62.5 MHz for 320 ms, which corresponds to approximately 14 rotor revolutions. At this measurement location of figure 23(a), 352 droplets were detected and plotted in the same graph.

In the last step of the post-processing routine the voltage signals of the valid droplets are converted to droplet diameters and speed and are plotted in a histogram distribution graph for each single measurement point. figures 26 and 27 show the droplet size and speed distributions respectively from the raw data file as presented in figure 23(a). The sample size for both distributions is 380. The three main parameters that can be extracted for the size are the D_{10}, D_{32} and D_{M} and for the velocity the average value V_{avg} as well as the most frequent value V_{M}.

5.2. Results for design and part load conditions at the location of x/c = 2%

In this paragraph the results for the design and part load conditions at $x/c = 2\%$ downstream of Stator 1 are presented. For this particular analysis the same circumferential traverse was chosen for both operating conditions. Figure 28 summarizes the droplet distribution diagrams at midspan location for these two operating conditions of the machine. Each plot contains the information of the Sauter mean diameter, the mode value as well as the mean value of the plotted distribution and the sample size of the distributions is 387 and 538 for Design and Part load speed condition respectively. The graphs highlight a skew normal distribution for all cases.

As depicted in figure 28, the droplet size is reduced by shifting the distributions to the left, with the increase of the relative flow velocity. In order to understand and describe the results, the Weber number We is introduced in equation (5). It is defined as the ratio of the dynamic pressure force to the surface-tension force acting on a drop and is a measure of the droplet stability for, i.e. the ability of the droplet to maintain a spherical geometry while shear forces try to tear it apart.

$$\mathrm{We} = \frac{D_d \cdot \rho_f \cdot \left|\overrightarrow{U_d} - \overrightarrow{U_f}\right|^2}{\sigma_d} \qquad (5)$$

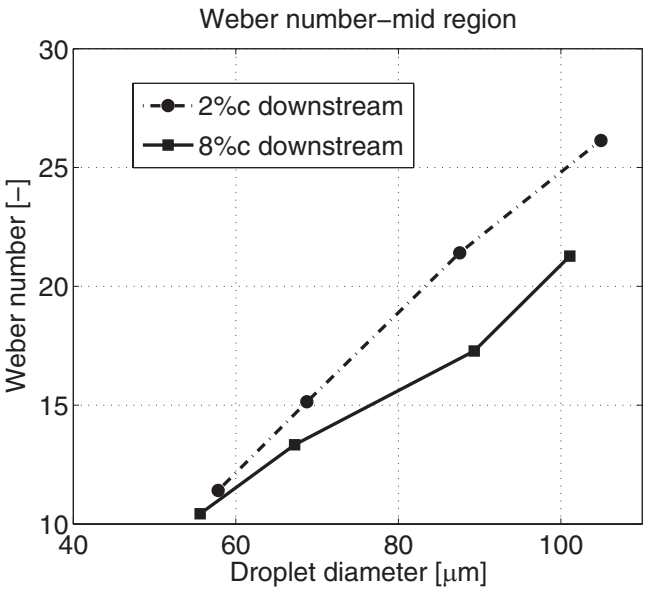

Figure 32. Weber number as a function of droplet diameter for the two different downstream axial locations of Stator 1.

When $\mathrm{We} \ll 20$ the droplets are spherical. As the Weber number increases and approaches the value of 20 to 23 the droplets begin to deform and eventually break up into smaller sizes [1, 40]. Applying this theoretical analysis to the current results, one can say that the main reason for the reduction of the droplet size from part load to the design operating condition, is due to the increase on the $\left|\overrightarrow{U_d} - \overrightarrow{U_f}\right|^2$ term of equation (5). As a consequence, higher shear forces between the flow and the droplets are generated which lead to greater values of Weber numbers resulting in the droplet's break up. Additional aerodynamic results can be found in [39] by Behr *et al*.

Many research studies address the significance of the droplet velocity magnitude relative to the rotor tip speed velocity [17, 41, 42]. This is due to the fact that the erosion rate on rotor blades is proportional to the droplet velocity and momentum described with a power law equation $R_e \sim U^n_{d,rel}$, where n is between 3–5 [41, 42] and is a factor which is material dependent. Figure 29 shows a schematic of the 2D velocity vectors at Stator 1 exit plane. As depicted in figure 29, the absolute droplet velocity ($U_{\mathrm{d,abs}}$) is assumed to have the same exit angle as the main absolute flow field angle ($U_{\mathrm{f,abs}}$) [30]. Following this assumption, the droplet relative velocity ($U_{\mathrm{d,rel}}$) can be calculated through the rotor rotational velocity ($U = \omega \mathrm{xr}$) for each radial location. The time averaged absolute flow yaw angle is 73.1° for design and 72.9° for part load conditions.

The results in figure 30(a) show that for both operating conditions the droplets ranging from 50 up to 100 μm diameter have, on an average, a deficit of 80% in absolute velocity compared to the flow. Therefore large water droplets ($D_{\mathrm{d}} > 80$ μm) will impact the rotor blade on the suction side of the leading edge. On the other hand figure 30(b) shows that the droplets' relative velocity is on an average 2 times larger for part load conditions compared to the design operating point. At part load condition the droplets in the range of 50

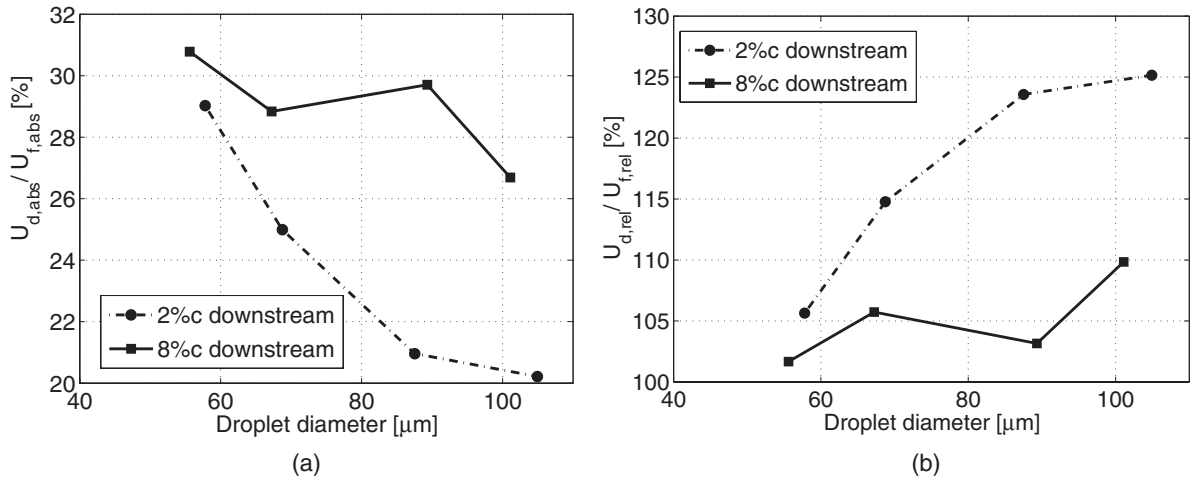

Figure 33. Absolute (a) and relative (b) droplet velocity at midspan location at $x/c = 2\%$ and 8% for part load condition.

μm in diameter have approximately the same relative velocity as the flowfield relative velocity ($U_{d,rel} \sim U_{f,rel}$) and the droplets at the range of 100 μm have 20% higher relative velocity compared to the flowfield relative velocity for the part load condition. For the design operating point there is no dependency between the relative droplet velocity and the droplet size, and the relative droplet velocity is 40% lower compared to the part load condition as shown in figure 30(b). The droplets will further accelerate due to aerodynamic drag forces and reach a maximum velocity depending on the available axial gap between stator and rotor blades [41, 43]. In order to further understand the formation mechanisms and be able to assess the droplets' maximum velocity before impacting the rotor leading edge, additional measurements were performed at a second location downstream of Stator 1.

5.3. Results for part load condition at locations of x/c = 2% and 8%

Since part load conditions have greater impact on the erosion mechanisms as shown in figure 30(b), only results from this operating point are presented in this paragraph for two different axial locations downstream of Stator 1. Figure 31 presents the droplet distribution at mid-span location for the part load condition at two locations downstream. The size distribution is 538 and 264 for 2%c and 8%c downstream. As shown in figure 31, the droplets' sizes reduce significantly as they accelerate from the stator trailing edge towards the rotor leading edge. This is expressed by the reduction on the actual value of the diameter as well as the reduction in detected coarse droplet count. The reduction of the Sauter Mean Diameter is 11.3%.

The velocity and the droplet size are the two main parameters affecting the erosion process at the rotor leading edge, as described previously. Thus, in order to verify the size of the droplets at the time they impact the rotor leading edge, the weber number as a function of droplet diameter is presented in figure 32. Measurements at 8%c downstream of Stator 1 show that the weber number is below the critical value of 22 for all droplet diameters. This implies that the droplets have reached a stable regime and they will not break up into smaller diameters.

The droplet speed results for the two downstream locations are presented in figures 33(a) and (b). As shown in figure 33(a) the droplets accelerate by 10% for the range of 50 μm in diameter and by 40% for the large range of 100 μm. Using the same assumptions as described in figure 29, the relative droplet diameter is calculated and plotted in figure 33(b). The droplets' relative speed is about 105% of relative flowfield velocity and roughly constant for all droplet sizes from 50 up to 100 μm in diameter. Having measured the current droplet speeds and diameter, according to the power law equation $R_e \sim U_{d,rel}^n$, the erosion rate at part load condition is increased exponentially and can reach from 16 up to 32 times higher depending on the blade material used for the rotor blades.

5.4. Time resolved results for design condition at x/c = 2%

The time-resolved droplet concentration downstream of Stator 1 is presented and discussed in the current paragraph. Figure 34 shows contour plots of the droplets' count distribution at the exit plane of Stator 1 over 4 rotor blade passing sub-periods equal to $t/T = 0.25$. In this case T is the respective rotor blade passing time period. It can be seen that the droplets' count distribution is modulated over a rotor blading passing period due to the flow field periodical interaction with the downstream rotor potential field as reported by Behr *et al* [39]. At $t/T = 0$ the rate obtains its maximum value of almost 120 drops/rev from 30% up to 90% span covering 20% of the stator pitch. At time $t/T = 0.25$ the droplet rate is reduced by 23% and as a consequence the actual area that the droplets cover is reduced, covering a lower range in spanwise and pitchwise direction. At $t/T = 0.5$ the droplet rate increases by 16%, which again results in the same increase on the area coverage and finally at time $t/T = 0.75$ the droplet rate increases and to get its maximum at $t/T = 0$. This implies that the potential flow field of the rotor blade as it crosses the stator trailing

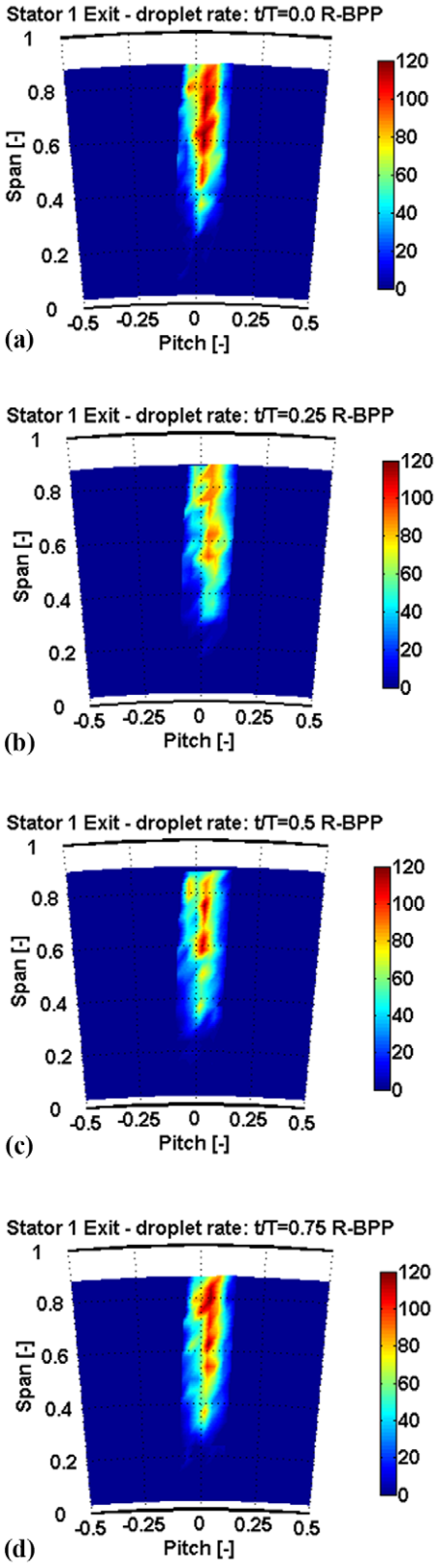

Figure 34. Time resolved droplet rate [droplets/rev] at Stator 1 exit plane for design point at four instants of the rotor blade passing period: (a) $t/T = 0.00$; (b) $t/T = 0.25$, (c) $t/T = 0.50$ and (d) $t/T = 0.75$.

edge generates a periodical fluctuation in the droplet impact rate with a variation of 15% around the mean value of 100 drops/rev.

6. Conclusions

A novel fast response optical backscatter probe has been designed, built and used in an axial turbine test facility. The novel miniature probe has a tip diameter of 5 mm and comprises of optical components for focusing a laser beam and collecting the backscattered light from droplets when crossing the probe's sample volume. The fast response photodiode used enables droplet measurements in the range of 40 to 110 μm in diameter in an environment with droplet concentration up to 10^{12} droplets m^{-3}. The design of the probe provides high spatial and temporal resolution suitable for unsteady measurements in the flow path of a large range of turbomachines.

In this paper the detailed calibration procedure is described as well. The calibration is conducted with a droplet generator capable of producing monodispersed water droplets from 40 to 110 μm in diameter. The measurement bandwidth of the new probe is 30 MHz, which is capable of resolving droplet speeds of up to Ma = 0.5. Substantial effort to reduce errors related to the operating principle of the probe was made. As presented in the current work, a correction routine to account for errors during measurements was developed. This sets the overall calculated uncertainty, accounting for all sources of errors for the diameter and speed measurements, to ± 4.7 μm and 2.3 m s^{-1} respectively. In addition, the probe is calibrated for droplet speed measurements and the results have shown that the effect on the entry angle of the droplet to the probe's sample volume can be neglected. Finally a post-processing algorithm to allow for droplet measurements in working environments with high surrounding noise is described. The developed routine increases the signal to noise ratio by a factor of 2, enabling accurate measurements in the low droplet range below 50 μm in diameter.

The application of the probe in the axial turbine test facility (LISA) has proven the robustness of the probe to provide reliable and accurate measurements under various operating conditions. Results have shown that when the airflow velocity increases the droplet diameter is reduced due to higher shear forces between the droplets and the stream flow. In addition, speed measurements showed that a part load condition results in an increase of relative droplet velocity by 40% compared to a design operating point, and that as a consequence, erosion can increase by up to 32 times. Finally, time resolved concentration measurements revealed an interaction of the stator droplet wake with the downstream rotor potential flow field with unsteady periodical fluctuations of up to 15%.

Acknowledgments

The authors would like to thank Mitsubishi Hitachi Power Systems, and more specifically Dr Shigeki Senoo for the financial and technical support provided over the course of the current project.

In addition the authors would like to acknowledge the support of Flori Alickaj for his contribution in the development of the FRAP-OB measurement system. Our appreciation also goes to Dr Kai Regina and Rainer Schaedler for their active support during the measurement campaign in the LISA facility.

References

[1] Lee Black D, McQuay M Q and Bonin M P 1996 Laser-based techniques for particle-size measurement: a review of sizing methods and their industrial applications *Prog. Energy Combust. Sci.* **22** 267–306

[2] Wendisch M, Keil A and Korolev A V 1996 FSSP Characterization with monodisperse water droplets *J. Atmos. Ocean. Technol.* **13** 1152–65

[3] Fugal J P, Shaw R A, Saw E W and Sergeyev A V 2004 Airborne digital holographic system for cloud particle measurements *Appl. Opt.* **43** 5987–95

[4] Ellis R A, Sandford A P, Jones G E, Richards J, Petzing J and Coupland J M 2006 New laser technology to determine present weather parameters *Meas. Sci. Technol.* **17** 1715

[5] Roques S 2007 An airborne icing characterization probe: nephelometer prototype *Smart Mater. Struct.* **16** 1784

[6] Lance S, Brock C A, Rogers D and Gordon J A 2010 Water droplet calibration of the cloud droplet probe (CDP) and in-flight performance in liquid, ice and mixed-phase clouds during ARCPAC *Atmos. Meas. Tech.* **3** 1683–706

[7] Baumgardner D *et al* 2011 Airborne instruments to measure atmospheric aerosol particles, clouds and radiation: a cook's tour of mature and emerging technology *Atmos. Res.* **102** 10–29

[8] Holve D and Self S A 1979 Optical particle sizing for *in situ* measurements part 1 *Appl. Opt.* **18** 1632–45

[9] Lemaitre P, Porcheron E, Grehan G and Bouilloux L 2006 Development of a global rainbow refractometry technique to measure the temperature of spray droplets in a large containment vessel *Meas. Sc. Technol.* **17** 1299

[10] Knox K J, Reid J P, Hanford K L, Hudson A J and Mitchem L 2007 Direct measurements of the axial displacement and evolving size of optically trapped aerosol droplets *J. Opt. A: Pure Appl. Opt.* **9** S180

[11] Dunn M G, Baran A J and Miatech J 1996 Operation of gas turbine engines in volcanic ash clouds *J. Eng. Gas Turbines Power* **118** 724–31

[12] White A J and Meacock A J 2004 An evaluation of the effects of water injection on compressor performance *J. Eng. Gas Turbines Power* **126** 748–54

[13] Kurz R and Brun K 2012 Fouling mechanisms in axial compressors *J. Eng. Gas Turbines Power* **134** 032401

[14] Reema K, Prasad J V R, Rajkeshar S, Swati S, Andy B-S and Tsuguji N 2014 Modeling and analysis of ice shed in multistage compressor of jet engines, presented at the *6th AIAA Atmospheric and Space Environments Conf.*

[15] Young J B, Yau K K and Walters P T 1988 Fog droplet deposition and coarse water formation in low-pressure steam turbines: a combined experimental and theoretical analysis *J. Turbomach.* **110** 163–72

[16] Dousti S, Cao J, Younan A, Allaire P and Dimond T 2012 Temporal and convective inertia effects in plain journal bearings with eccentricity, velocity and acceleration *J. Tribol.* **134** 031704

[17] Cai X *et al* 2014 Coarse water in low-pressure steam turbines *Proc. Inst. Mech. Eng.* A **228** 153–67

[18] Walters P and Skingley P 1979 An optical instrument for measuring the wetness fraction and droplet size of wet steam flows in LP turbines *Proc. Inst. Mech. Eng.* C **141** 337–48

[19] Tatsuno K and Nagao S 1986 Water droplet size measurements in an experimental steam turbine using an optical fiber droplet sizer *J. Heat Transfer* **108** 939–45

[20] Walters P T 1987 Wetness and efficiency measurements in LP Turbines with an optical probe as an aid to improving performance *J. Eng. Gas Turbines Power* **109** 85–91

[21] Cai X, Ning T, Niu F, Wu G and Song Y 2009 Investigation of wet steam flow in a 300 MW direct air-cooling steam turbine. Part 1: Measurement principles, probe, and wetness *Proc. Inst. Mech. Eng.* A **223** 625–34

[22] Hayashi K, Shiraiwa H, Yamada H, Nakano S and Tsubouchi K 2011 150 kW Class two-stage radial inflow condensing steam turbine system *ASME 2011 Turbo Expo: Turbine Technical Conf. and Exposition* pp 211–20

[23] Kercel S W, Simpson M L, Azar M and Young M 1993 An optical technique for characterizing the liquid phase of steam at the exhaust of an LP turbine *Office of Scientific and Technical Information (OSTI) Report* vol 24

[24] Schatz M and Casey M 2007 Design and testing of a new miniature combined optical/pneumatic wedge probe for the measurement of steam wetness *AIP Conf. Proc.* **914** 464–79

[25] Fan X, Jia Z, Zhang J and Cai X 2009 A video probe measurement system for coarse water droplets in LP steam turbine *J. Phys.: Conf. Ser.* **147** 012065

[26] Bosdas I, Mansour M, Kalfas A, Abhari R and Senoo S 2015 *Unsteady Wet Steam Flow Field and Droplet Measurements at the Last Stage of Low-Pressure Steam Turbine*, presented at the IGTC, Tokyo, Japan

[27] Laven P *Mie Plot* Available: www.philiplaven.com (accessed November 2013)

[28] Avellan F and Resch F 1983 A scattering light probe for the measurement of oceanic air bubble sizes *Int. J. Multiph. Flow* **9** 649–63

[29] Baumgardner D, Strapp W and Dye J E 1985 Evaluation of the forward scattering spectrometer probe. Part II: corrections for coincidence and dead-time losses *J. Atmos. Ocean. Technol.* **2** 626–32

[30] Crane R I 2004 Droplet deposition in steam turbines *Proc. Ins. Mech. Eng.* C **218** 859–70

[31] Martinez F, Velazquez M, Silva F, Martinez A, Montes S and Chavez O 2011 Theoretical and numerical analysis of the mechanical erosion in steam turbine blades. Part I *Energy Power Eng.* **03** 227–37

[32] Kleitz A and Dorey J M 2004 Instrumentation for wet steam *Proc. Ins. Mech. Eng.* C **218** 811–42

[33] Petr V and Kolovratnik M 2000 Modelling of the droplet size distribution in a low-pressure steam turbine *Proc. Ins. Mech. Eng.* A **214** 145–52

[34] Cai X, Niu F, Ning T, Wu G and Song Y 2010 An investigation of wet steam flow in a 300MW direct air-cooling steam turbine. Part 3: heterogeneous/homogeneous condensation *Proc. Ins. Mech. Eng.* A **224** 583–9

[35] Korolev A, Shashkov A and Barker H 2013 Calibrations and performance of the airborne cloud extinction probe *J. Atmos. Ocean. Technol* **31** 326–45

[36] Rollinger B, Morris O and Abhari R S 2011 Stable tin droplets for LPP EUV sources *Proc. SPIE* **7969** 79692W

[37] Damaschke N, Nobach H, Semidetnov N and Tropea C 2002 Optical particle sizing in backscatter *Appl. Opt.* **41** 5713–27

[38] ISO Guide 98 1995 *Guide to the Expression of Uncertainty in Measurement (GUM)* (International Organisation for Standardization)

[39] Behr T, Kalfas A I and Abhari R S 2007 Unsteady flow physics and performance of a one-and-1/2-stage unshrouded high work turbine *ASME J. Turbomach.* **129** 348–59

[40] Ow C S and Crane R I 1979 On the critical weber number for coarse water formation in steam turbines *J. Mech. Eng. Sci.* **21** 353–6

[41] Lam T C T and Dewey R 2003 A Study of droplet erosion on two L-0 turbine stages *Int. Joint Power Generation Conf.* (Atlanta USA)

[42] Ahmad M, Casey M and Sürken N 2009 Experimental assessment of droplet impact erosion resistance of steam turbine blade materials *Wear* **267** 1605–18

[43] Eisfeld T and Joos F 2009 Experimental investigation of twophase flow phenomena in transonic compressor cascades *ASME Turbo Expo 2009: Power for Land, Sea and Air* pp 103–12